Home   Search   Collections   Journals   About   Contact us   My IOPscience

Dynamic characterization of contact interactions of micro-robotic leg structures

You may also be interested in:

Model identification for impact dynamics of a piezoelectric microactuator
Jeong Hoon Ryou and Kenn Richard Oldham

Quadrupedal galloping control for a wide range of speed via vertical impulse scaling
Hae-Won Park and Sangbae Kim

Design and control of a bio-inspired soft wearable robotic device for ankle--foot rehabilitation
Yong-Lae Park, Bor-rong Chen, Néstor O Pérez-Arancibia et al.

Bioinspired legged-robot based on large deformation of flexible skeleton
Mohammad Mayyas

Design and vibration analysis of a piezoelectric-actuated MEMS scanning mirror and its application
to laser projection
Chung-De Chen, Yao-Hui Lee and Chien-Shien Yeh

A small biomimetic quadruped robot driven by multistacked dielectric elastomer actuators
Canh Toan Nguyen, Hoa Phung, Tien Dat Nguyen et al.

Millipede-inspired locomotion through novel U-shaped piezoelectric motors
Dragan Avirovik, Bryan Butenhoff and Shashank Priya

An electro-mechanically coupled model for the dynamic behavior of a dielectric electro-active
polymer actuator
M Hodgins, G Rizzello, D Naso et al.

Modeling, simulation and measurement of the dynamic performance
Z J Guo, N E McGruer and G G Adams

Dynamic characterization of contact interactions of micro-robotic leg structures

Jeong Hoon Ryou and Kenn Richard Oldham

Department of Mechanical Engineering, University of Michigan, 2350 Hayward, Ann Arbor, MI 48109, USA

E-mail: jhryou@umich.edu and oldham@umich.edu

Abstract
Contact dynamics of microelectromechanical systems (MEMS) are typically complicated and it is consequently difficult to model all dynamic characteristics observed in time-domain responses involving impact. This issue becomes worse when a device, such as a mobile micro-robot, is not clamped to a substrate and has a complex mechanical structure. To characterize such a contact interaction situation, two walking micro-robot prototypes are tested having intentionally simple structures with different dimensions (21.2 mm × 16.3 mm × 0.75 mm and 32 mm × 25.4 mm × 4.1 mm) and weights (0.16 and 2.7 g). Contact interaction behaviors are characterized by analyzing experimental data under various excitation signals. A numerical approach was used to derive a novel contact model consisting of a coefficient of restitution matrix that uses modal vibration information. Experimental validation of the simulation model shows that it captures various dynamic features of the contact interaction when simulating leg behavior more accurately than previous contact models, such as single-point coefficient of restitution or compliant ground models. In addition, this paper shows that small-scale forces can be added to the simulation to improve model accuracy, resulting in average errors across driving conditions on the order of 2–6% for bounce frequency, maximum foot height, and average foot height, although there is substantial variation from case to case.

Keywords: MEMS, micro-robotics, contact dynamics, dynamic modeling

(Some figures may appear in colour only in the online journal)

1. Introduction

Terrestrial micro-robots, like their macro-scale counterparts, may draw benefits in terms of speed and energy consumption from dynamic walking or running gaits. However, there are few studies directly applicable to the modeling of contact dynamics during interactions between the ground and micro-robots with dimensions smaller than a few tens of millimeters. One factor in this is that the dynamics of walking robots become especially complicated due to scaling effects that significantly increase the influence of inter-surface interactions on system dynamics. This can give rise to discrete, irregular and unpredictable impact disturbances generated by contact between the feet and the ground. Thus, the majority of micro-robots undergoing vertical foot contact and release [1–3] have been limited to quasi-static walking gaits. Previous micro-robots where dynamic ground effects have influenced motion have relied only on friction effects during stick–slip [4] and electrostatic scratch drive [5] actuation.

The modeling of dynamic vertical contact between micro-robot feet and the ground has not been previously studied, though it may have use in developing dynamic micro-robot walking or running gaits. The simple robots for which contact modeling is performed here are driven by piezoelectric actuators. Piezoelectric actuation has been used or proposed for previous swimming [6–8] and flying [9, 10] milli- or micro-robots, but these robots do not experience impact events of the type incurred during terrestrial locomotion. Previous small terrestrial piezoelectric robots are about an order of magnitude in mass larger than the smaller robot studied in this

paper, and experience much more uniform contact dynamics than are observed in the current work [11].

More directly relevant prior studies arise in other situations involving contact between structures, and can be sorted into two primary groups: contact dynamic modeling of macro-scale walking robotic systems and contact dynamics in other microelectromechanical systems (MEMS).

First, walking analysis based on a contact model in a macro-system structure has been approached using several representative contact models. These include coefficient of restitution models [12], continuous contact force models [13], and a planar kinematic chain with a compliant ground model [14]. Unfortunately, these are difficult to apply to micro-scale walking robots. A common feature of these models is that impact influence is estimated using only states associated with the physical point where contact occurs. However, small micro-devices typically consist of continuous, compliant structures that may be affected throughout the whole structure by external impact over a very short time period. Adjusting only where contact physically occurs is not efficient in capturing the influence of contact on the system dynamics, as will be discussed in more detail later in this paper.

Second, micro-scale contact dynamics have been investigated for other MEMS devices, such as atomic force microscopy (AFM) probes [15], micro-mirrors [16], and micro-switches [17]. The variety and history of these studies imply that the influence of various nonlinear contact forces on the device operation is significant in the micro-scale environment. Also implied is that it is by no means straightforward to characterize contact dynamics even when the structures of such devices are relatively simple and the structure is partially fixed, or clamped, to the substrate. Attempting to generalize the methodology for modeling contact dynamics of such typical MEMS beam-shaped devices to a lumped-parameter model convenient for micro-robot modeling, the authors previously proposed a modeling procedure for a piezoelectrically operated micro-cantilever under repetitive contact interactions [18]. However, the studies mentioned above are not fully applicable to walking micro-robots, either. Due to mobility, walking micro-robots do not necessarily have a fixed or stationary point in the system with respect to the ground, and impact forces are difficult to predict or measure directly. Meanwhile, structural modeling of robot dynamics can include many vibration modes and their modeling must accommodate short timescale events at impact and longer term dynamics over many steps, which can be difficult to achieve with existing impact models. Due to these features the contact interactions in these comparatively unconstrained and small-scale actuation structures will be seen to be more chaotic, complicated, and thus hard to characterize with contact dynamic models introduced in the studies listed above.

In this work, we propose an alternate form for modeling contact dynamics between a micro-robot foot and the ground using experimental analysis to derive an expanded coefficient of restitution (CoR) matrix. This model provides a fair estimation of robot motion over various test scenarios without specified geometry or ground material.

During this analysis, we tested two robotic structures with different dimensions and shapes, shown in figure 1. The
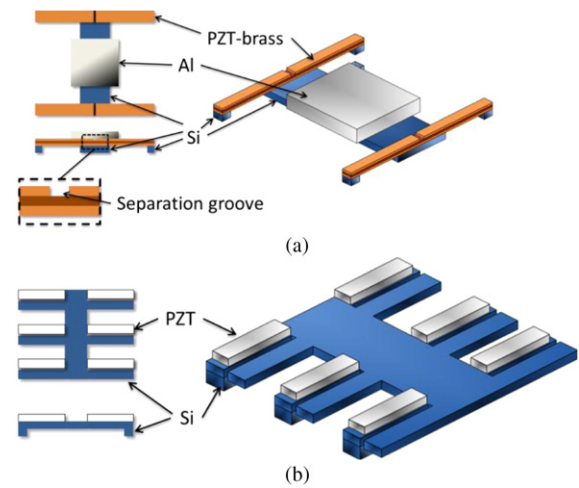
Figure 1. Micro-robot prototypes based on bulk PZT ceramics: (a) the quadruped bulk PZT robot (QBPZTR) is based on assembly of off-the-shelf PZT bimorphs to machined silicon and aluminum components, (b) the hexapod bulk PZT robot (HBPZTR) is based on direct assembly of small PZT ceramic strips to a micro-machined silicon chassis and leg structure.

smaller of the robots was also used to estimate the magnitude of other small-scale forces between surfaces at short range, such as electrostatic attraction and squeeze-film damping. Using experimental comparisons, the proposed modeling method will be validated and discussed. The proposed modeling method is expected to be applicable to similar microstructures that are best modeled as continuous, modal structures with specific points of contact with their surroundings.

2. Experimental methods

2.1. Test devices

Two micro-robotic prototypes, shown in figure 1, are tested to evaluate possible models for their contact behaviors. Both prototypes are actuated by bulk lead–zirconate–titanate (PZT) ceramics; one is referred to as a quadruped bulk PZT robot (QBPZTR) and the other as a hexapod bulk PZT robot (HBPZTR). These robot geometries are designed to have comparatively simple continuous structures to illustrate fundamental dynamic behavior for potential application to other micro-robotic structures with similar sizes. Their structure is intended to also reduce complexity in modeling system dynamics so that the influences of contact on a system can be characterized more easily. These robots have leg structures with thicknesses of $100–250\ \mu$m and maximum robot lengths on the order of 2 cm. They are strong enough to endure repetitive tests on impact with various ground surfaces but have small enough dimensions and inertia for the effects of various short-range forces to be observed.

As shown in figure 1, the QBPZTR was assembled with two PZT–Brass–PZT (STEMINC SMBS1515T06P750) composite strips attached to a silicon piece which is mounted on an aluminum block to reduce the influence of wire tethers on robot motion. By etching the electrodes on the PZT, each strip can be operated as two separate legs. For the HBPZTR, $150\ \mu$m thick PZT ceramic blocks (Naval Type VI, cut to shape by a
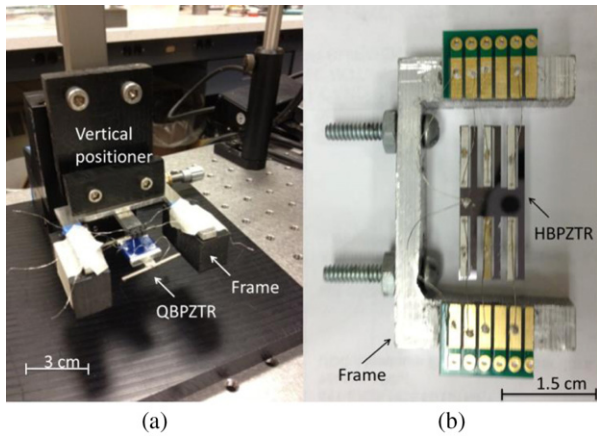
Figure 2. Example photographs of the test prototypes: (a) QBPZTR and (b) HBPZTR in testing fixtures for vertical motion measurement.

Figure 3. Test setup for manipulating gap distances between test devices and ground pad: (a) components and (b) fully assembled.

silicon dicing saw) were attached to a bulk micro-machined silicon structure using conductive epoxy. In this configuration, the PZT strips function as actuators while most of leg structure is composed of silicon. Both robots have additional 'feet', either bulk micro-machined or attached by adhesive beneath the tips of legs to better approximate full-fledged walking micro-robots, and also to allow for a large degree of lumped-parameter modeling of foot-interaction characteristics with a reduction of structural modeling complexity. Figure 2 shows two example photographs of the completed robot prototypes.

Only vertical motion is focused on in this work. This is in part due to limitations on experimental equipment, but also because we see the first task in understanding micro-robot foot–terrain interactions to be analyzing the bouncing, firm contact, and/or sticking of micro-robot feet during vertical motion. Based on this assumption, the QBPZTR was designed from the beginning to have vertical motion only. In quasi-static operation, when a voltage is applied, the difference in extended lengths between the PZT layers and the brass layer at the middle of the leg causes the tip of the leg to bend up and down, creating foot motion. On the other hand, the smaller HBPZTR was originally designed to have both vertical and lateral motions at the tip of the leg. However, in this paper, the 'shin' part below the thigh for each leg is simply cut off and an additional 'foot' silicon cube is attached to the bottom of the remaining leg tip, leaving only vertical motion for the HBPZTR, as well.

2.2. Test setup and experimental procedure

Contact or impact behavior in a mechanical structure is generally complicated and becomes even more so when structures are not clamped to any fixed body but are freely movable in space. Thus, the structural dynamics are characterized first, without contact, for later use in modeling dynamic behaviors with ground contact. Using wires connected to power sources, both of the test devices are suspended in the air. A thin copper wire (MIL-W-16878/4) is used and only a single strand (0.20 mm) is extracted and attached in order to reduce the influence of wires on dynamics of the robots. An adjustable-height
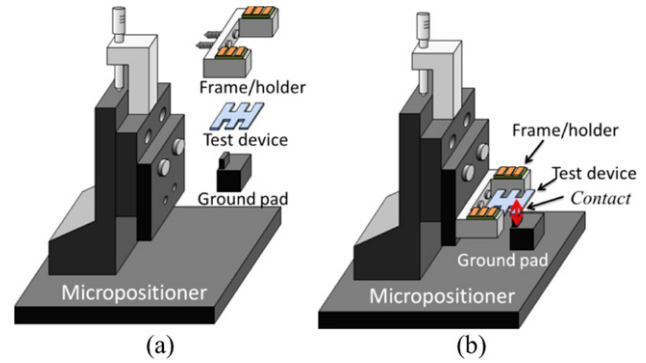
micro-positioner allows testing at various robot heights above the ground and for various ground materials to be inserted underneath the robot foot. Figure 3 shows the complete test apparatus; by adjusting the height of the robots, a very narrow gap with a range of 10–30 μm between a foot and a ground pad can be achieved. This enables analysis of system responses over various gap lengths for the characterization of small-scale forces such as squeeze-film damping or electrostatic attraction. This is useful because the small-scale forces are often highly sensitive to the gap between surfaces [18, 19].

Out-of-plane motion was measured using a laser Doppler vibrometer (Polytek PSV-400), as shown in figure 4(a). Vertical motion measurements were taken in three positions, corresponding to three stages of analysis:

(1) Suspended in air, without the influence of disturbances from the ground, for use in modeling of structural dynamics of the test devices by modal analysis with sinusoidal and square wave excitations at various frequencies (section 3.1).

(2) During intermittent or periodic contact with the ground pad, for use in developing a contact model of robot leg impact. Contact interactions with various initial gaps between a foot and a ground pad were created by adjusting the height of the robots using the micro-positioner shown in figure 3. For simplicity, only single foot–ground interactions are tested and studied in this paper. Various sinusoidal and square wave excitations were applied for use in modeling and validation (sections 3.2–3.4).

(3) In close proximity with the ground pad but without contact, once the position at which contact occurs was known, for use in quantifying small-scale forces (section 3.5).

3. Analytical methods

3.1. Robot structural modeling

Structural dynamics of the robots in the absence of impact are modeled entirely empirically, following the modal identification method of Inman [20]. Dynamics for the robots are represented with linear-time-invariant (LTI) modal models of five degrees and six degrees of freedoms for QBPZTR and HBPZTR, respectively. Model order was selected according
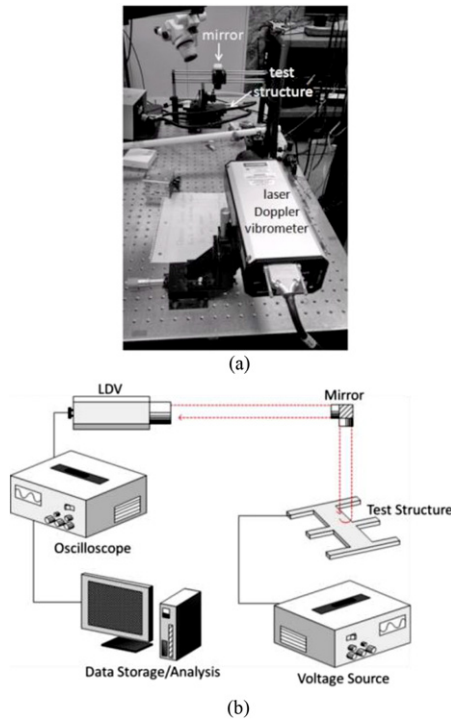
Figure 4. Measurement instruments and setup: (a) photograph of the laser Doppler vibrometer setup and (b) schematic view.

Table 1. Resonance frequencies of tested robots.

Resonance frequencies (Hz)	HBPZTR	QBPZTR
ω_1	89.5	15.0
ω_2	134.0	86.0
ω_3	314.6	181.0
ω_4	368.5	724.0
ω_5	660.0	893.0
ω_6	2910	—

to the number of major resonance modes needed to capture dynamic characteristics in air of each device. Operating frequencies ranged from 10 to 5000 Hz. The identified resonances are shown in table 1, and are used in further system identification and the simulation model.

Based on the measured data, modal identification was conducted. The robots' dynamic equations of motion were computed in terms of a modal coordinate displacement vector, **q**,

$$\ddot{\mathbf{q}} + \mathbf{\Lambda_C}\dot{\mathbf{q}} + \mathbf{\Lambda_K}\mathbf{q} = \mathbf{Bu} \tag{1}$$

where $\mathbf{\Lambda_C}$ and $\mathbf{\Lambda_K}$ are diagonal matrices of modal damping terms and squared natural frequencies, respectively. The term on the right hand side of (1) indicates a driving force where **u** is a vector of inputs to legs and **B** represents the input matrix that sums the effects of external forces on each mode. For a given selection of measured displacements at specific locations on the robot structure, a transformation matrix **Φ** may be applied to produce the summation of modal contributions at each location $\mathbf{x} = \mathbf{\Phi}\mathbf{q}$. The matrix **Φ** can be conceptually defined as

$$\mathbf{x} = \mathbf{\Phi}\mathbf{q} = (\mathbf{M}^{-1/2}\mathbf{P}\eta_0)\mathbf{q} \tag{2}$$

where **M** is an equivalent mass matrix and **P** is a normalized matrix of eigenvectors of the matrix $\mathbf{M}^{-1/2}\mathbf{K}\mathbf{M}^{-1/2}$, with **K** an equivalent mass matrix. Scalar η_0 is an arbitrary constant with units of 1/mass. Applying (2) to (1) and pre-multiplying by $\eta_0(\mathbf{P}^{-1})^{\mathrm{T}}\mathbf{M}^{1/2} = \mathbf{\Phi}^{\mathrm{T}}$ produces a standard mass-damping-stiffness form

$$\mathbf{M}\ddot{\mathbf{x}} + \mathbf{C}\dot{\mathbf{x}} + \mathbf{K}\mathbf{x} = \mathbf{F} \tag{3}$$

where **C** is an equivalent damping matrix and **F** is a distributed force vector. For the QBPZTR, **x** is a 5-by-1 vector representing vertical positions of four feet and the center of body. For the HBPZTR, **x** is represented a 6-by-1 vector of the six foot positions. For the micro-robots, **F** can be divided into the driving force, $\mathbf{F_D}$, impact force, $\mathbf{F_I}$, and small-scale non-contact forces, $\mathbf{F_{SS}}$,

$$\mathbf{F} = \mathbf{F_D} + \mathbf{F_I} + \sum \mathbf{F_{SS}}. \tag{4}$$

Experimentally, the natural frequencies and damping terms in (1) and modal gains in **B** and **Φ** are obtained by the circle fit method and proceeding analysis in [21]. **M**, **C**, **K** and **F** are not uniquely known without knowledge of the amplitude of at least one of their terms, with $\mathbf{F_D}$ being known in the case of the micro-robots. The use of the scaling factor η_0 as done here is not standard, but rather done for convenience to make **Φ** dimensionless, allowing later impact analysis to be done using the same units in physical and modal coordinates.

With respect to the assumption of input linearity, since less than 10% of the maximum allowable voltage for the bulk PZT ceramics is applied, piezoelectric hysteresis is neglected, with the experimentally measured output foot displacement versus input voltage showing less than 1% error compared to perfect linear outputs. Figure 5 shows the variability between resonance frequency measurements taken at different points on a robot, and a comparison between simulated and experimental leg amplitude versus voltage without any foot–terrain interaction and large distances from the ground. These comparisons indicate that there is some uncertainty in the exact resonance frequency measurement, but linearity of the actuators at low voltages is very good.

3.2. Limitations of conventional impact models

Once a structural model was obtained, contact between the robot foot and ground was introduced, and used to compare existing and proposed contact models. In this section, sample responses of the experimental system are presented, and compared to simulated behavior using existing contact models. The existing contact models evaluated were the single CoR approach and a compliant ground model approach.

First, it is important to highlight that motion of the robots with ground contact is observed to be very complicated even under single-point contact interaction with pure sine/square voltage inputs, as shown in figure 6. No strictly periodic steady-state outputs of a linear system are observed even with a considerable operation time, such as an hour. However, motion is bounded and quasi-repetitive over multiple periods. Based on such regularity, it was hypothesized that it would be possible

(a)

(b)
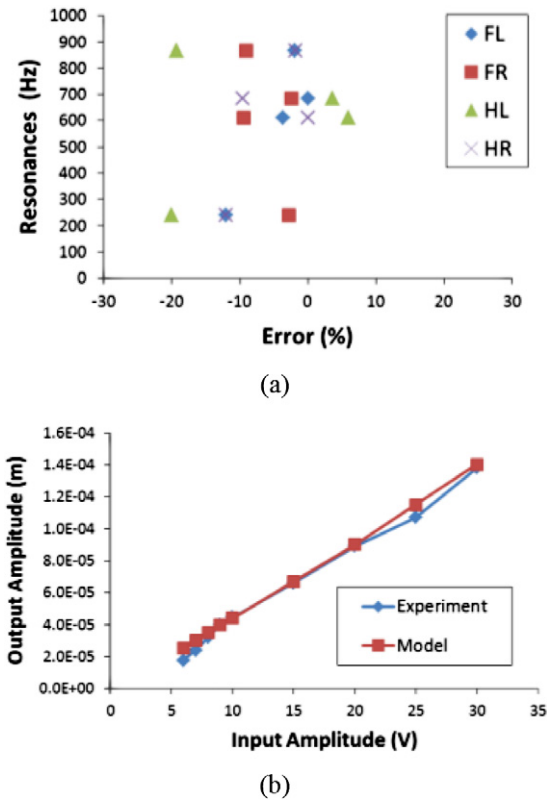
Figure 5. Error of structural models without contact shows good agreement between linear modal vibration modeling and the experimental result: (a) error percentages between experimental data and simulations at modal driving frequencies are on the order of −20% to 5% (QBPZTR) (FL: fore-left foot, FR: fore-right foot, HL: hind-left foot, HR: hind-right foot); (b) input amplitudes versus output amplitudes for both experimental data and simulations show linearity of the input signal (HBPZTR).

to estimate impact behavior and apply it to the linear structure models derived in the previous section.

A major challenge for modeling is that complicated behavior is observed not only in the motion of the leg interacting with the ground but also those legs moving only in air. That is, the motion all legs changes significantly when there are impact disturbances into the system at other legs. Contributing factors to this behavior are that:

- Small micro-devices can be affected throughout the whole structure by external impact over a very short time period, due to their continuous, low-mass structure.
- Contact interactions also induce low-frequency modes, including rigid body modes related to the wire bonding of the tethered robots.
- Being suspended in air may result in modal vibrations being sustained over time which are more rapidly damped out in other circumstances.

To evaluate whether these effects could be reproduced by existing contact models, simulation was performed with a simple coefficient of restitution (CoR) applied to the foot contacting with the ground. Supposing a model considers $n+1$
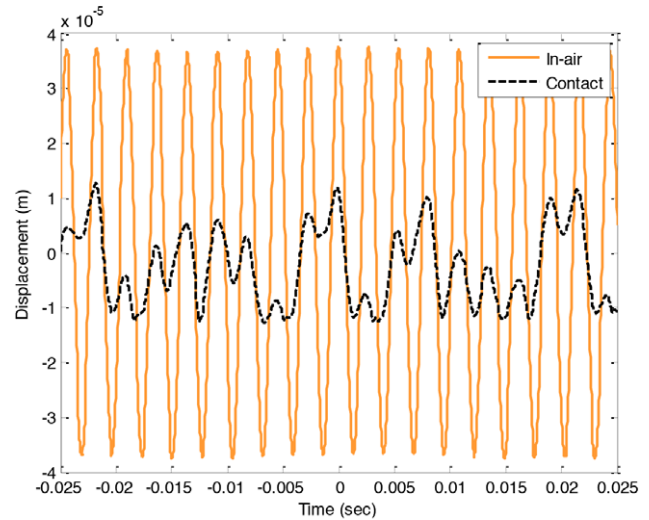
Figure 6. System responses at the tip of a leg with/without single contact interaction (10 V, sine waveform input, ∼25 μm gap, HBPZTR).

positions of a test system, at the moment of contact, $t = t_c$,

$$
\begin{bmatrix}
\dot{x}_c(t_c^+) \\
\dot{x}_1(t_c^+) \\
\vdots \\
\dot{x}_n(t_c^+)
\end{bmatrix}
=
\begin{bmatrix}
-\alpha \dot{x}_c(t_c^-) \\
\dot{x}_1(t_c^-) \\
\vdots \\
\dot{x}_n(t_c^-)
\end{bmatrix}
\tag{5}
$$

where x_c represents the position for the foot making contact with the ground and α is the CoR at that point. As shown in figure 7(a), it is difficult to use a single CoR method to model observed behavior without excessively small simulation time steps. In the case shown, the system response diverged in the simulation even with a very small time step of 10^{-15} s, which is much shorter than the conventionally used critical value of $2/\omega_M$, where ω_M is the maximum fundamental frequency considered in the model (about 2911 Hz for HBPZTR and 893 Hz for QBPZTR). Any attempted values for both the CoR and the simulation time step resulted in the foot displacement being either divergent or converging to 0.

The difficulty in applying a single CoR approach to this situation is attributed to the fact that it is not adequate to capture the contact behavior by adjusting only the state involved in the contact point at the instant of contact for such a very small system. In fact, as shown in figure 8, there are severe changes in other idle legs within extremely short time durations following impact and it is hard to capture this in simulation by adjusting only the leg interacting with the ground.

A similar challenge is found in using a compliant ground model to simulate robot behavior. As shown in figure 7(b), in this case, the failure to accommodate changes over the entire structure in a short time period causes important variation to be lost in simulation. The ground compliance leads to a much more uniform dynamic response than is observed experimentally. The limitations of the above two methods suggest that other contact models dealing only with the contact point, such as certain modal coordinate approaches [21], would be unable to predict experimental behavior as well.

5
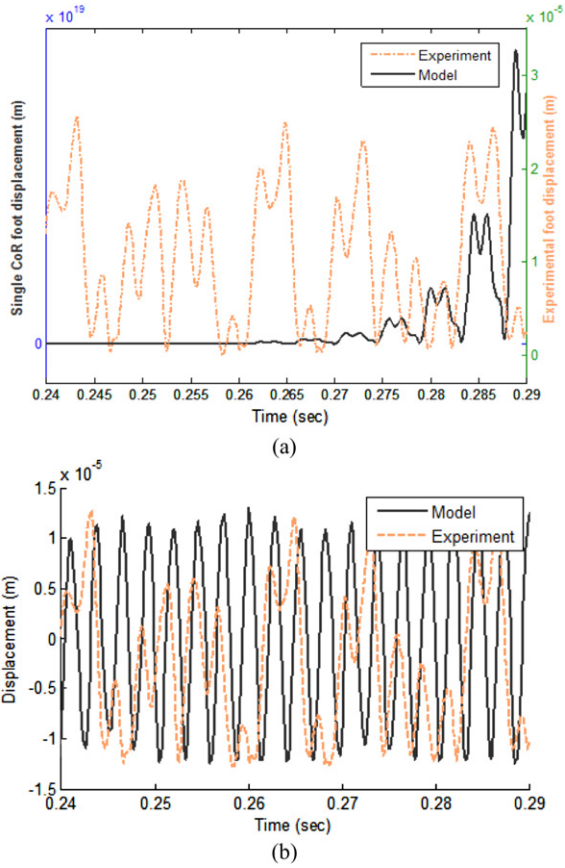
Figure 7. Simulation results with conventional contact/impact models: (a) single coefficient of restitution, (b) compliant ground model.
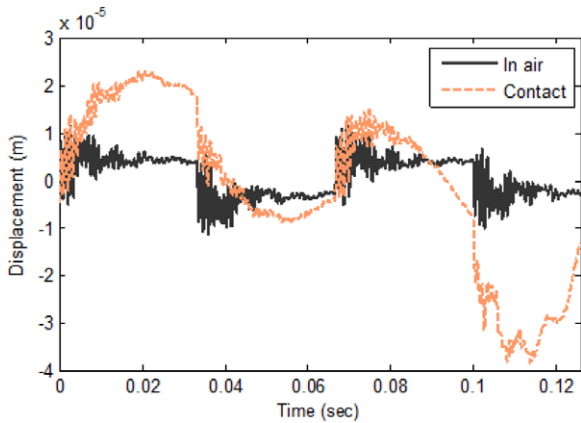
Figure 8. Idle leg response comparison example with/without contact interaction (fore-right leg of QBPZTR).

3.3. Contact data analysis

Noting that conventional contact models were not successful in predicting the complex contact behavior seen experimentally, we carried out analysis on the experimental data to find trends for its characterization. First, it was observed that the computed CoR values at the contact point are relatively consistent over various voltage inputs for both robotic structures, as shown in figure 9. The estimated CoR at the contact point at each
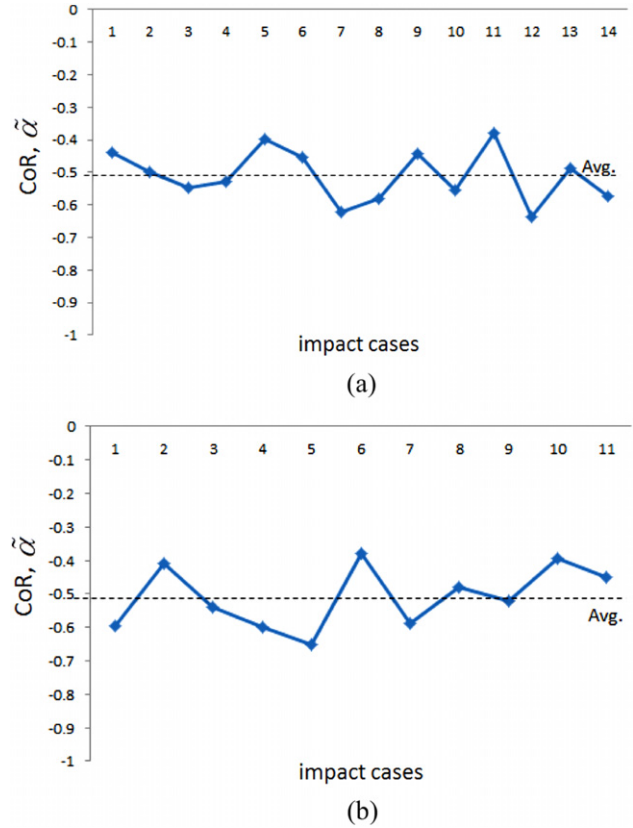
Figure 9. Computed CoR over various experimental data: (a) HBPZTR, (b) QBPZTR.

Table 2. Tested periodic voltage input signals.

	QBPZTR	HBPZTR
Waveform	Sine/square	Sine/square
Frequency range (Hz)	15–1000	20–900
Voltage range (V)	2–10	3–30

impact, $\tilde{\alpha}$, is computed as

$$\tilde{\alpha} = \frac{\dot{\tilde{x}}_c^+}{\dot{\tilde{x}}_c^-} \qquad (6)$$

where $\dot{\tilde{x}}_c^-$ and $\dot{\tilde{x}}_c^+$ are the measured velocities of the foot immediately before and after impact with the ground. The periodic voltage input signals used here are shown in table 2. As can be seen, the experimental value for a CoR is not perfectly constant, it varies over a relatively narrow range of -0.51 ± 0.11 for both robots on a silicon substrate.

However, as noted above, inserting a CoR model at the contact foot alone does not adequately predict motion at other locations of the robotic structure. Further trends in impact behavior were identified by numerical analysis of the experimental data. This showed several further quantities having significant regularity in impact behavior. The quantities showing such consistencies include: the ratio of the modal velocity changes at impact to the contact foot velocity right

(a)

(b)

(c)
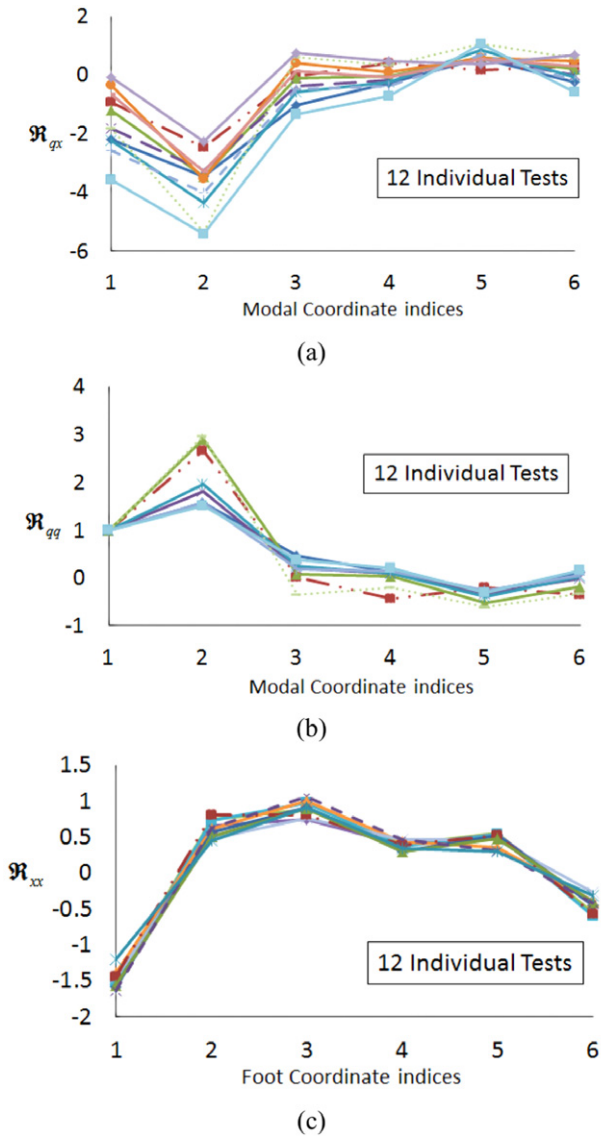
Figure 10. Various ratios between coordinate velocity changes at impact remain consistent over many impacts, notably: (a) ratio of modal velocity changes at impact to the contact foot velocity right before impact, $\Re_{qx}$; (b) ratio of modal velocity changes at impact to the first mode velocity right before impact, $\Re_{qq}$; (c) ratio of foot velocity changes at impact to the contact foot velocity right before impact, $\Re_{xx}$.

before impact; the ratio of the modal velocity changes at impact to the first mode velocity change at impact; and the ratio of the foot velocity changes at impact to the contact foot velocity right before impact. These quantities, labeled $\Re_{qx}$, $\Re_{qq}$ and $\Re_{xx}$, respectively, are shown in figure 10 and were obtained by the following calculations:

$$\Re_{qx} = \Delta\dot{\tilde{\mathbf{q}}}/\dot{\tilde{x}}_c^- \qquad (7)$$

$$\Re_{qq} = \Delta\dot{\tilde{\mathbf{q}}}/\Delta\dot{\tilde{q}}_1 \qquad (8)$$

$$\Re_{xx} = \Delta\dot{\tilde{\mathbf{x}}}/\dot{\tilde{x}}_c^- \qquad (9)$$

where $\Delta\dot{\tilde{\mathbf{q}}}$ indicates a vector of the measured modal velocity changes at impact, $\Delta\dot{\tilde{q}}_1$ the first modal velocity change at impact, and $\Delta\dot{\tilde{\mathbf{x}}}$ the vector of the foot velocity changes at impact.
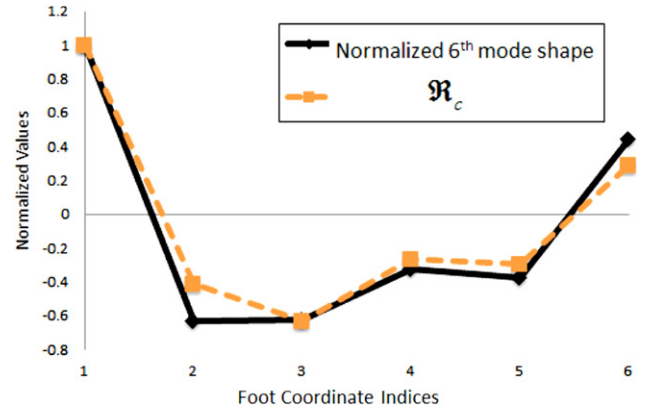
Figure 11. The change in foot coordinate velocities observed experimentally can be described almost entirely by the mode shape of mode 6, as seen in this comparison between the averaged $\Re_c$ and the sixth mode shape vector of HBPZTR.
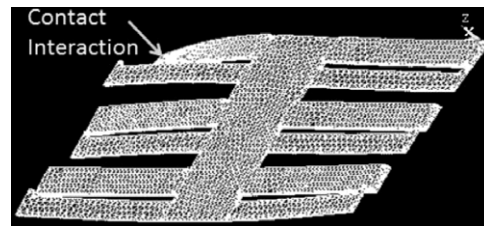
Figure 12. Deformed shape of an ideal ANSYS model of HBPZTR shows the dominant deflection of the contact foot in the sixth mode shape.

The most notable observed characterization was $\Re_{xx}$, which, as illustrated in figure 10(c), showed an especially consistent behavior across all excitation scenarios. Given this consistency over the various test cases, it was hypothesized that this might be due to structural characteristics of the test device, which was likewise indicated by comparison with the essential mode shapes of the device. Normalizing $\Re_{xx}$ with its first element, a new quantity, $\Re_c = \Delta\dot{x}/\Delta\dot{x}_c^-$ can be obtained, that shows the same relationship as the normalized mode shape. This is shown in figure 11 for the sixth mode in the dynamic model of the HBPZTR. As each mode represents a specific deformed structure, such as shown in figure 12 for the sixth mode of the HBPZTR, this confirms that the core characteristics of impact behavior are strongly related to structural characteristics.

This analysis was also conducted on the QBPZTR and the result, as shown in figure 13, also indicated that experimental responses could be largely attributed to a single vibration mode, even when piezoelectric forcing occurs at other frequencies. Based on this experimental data analysis from both of the test devices, it was established that the impact behavior is related to structural characteristics, which is an expected outcome, and that it can be represented by one major resonance mode of the structure.

3.4. Impact model

To justify this experimental observation and the established hypothesis theoretically, mathematical development was
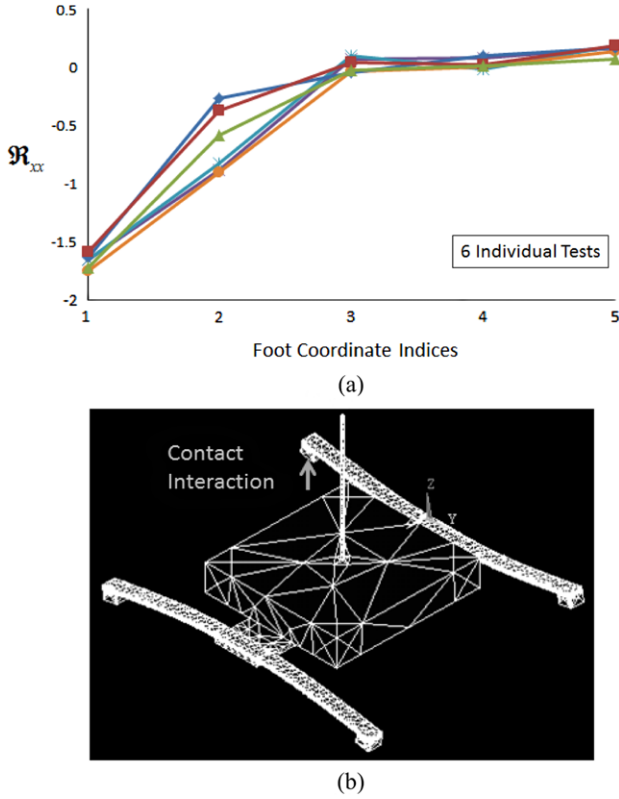
Figure 13. Consistent trend in impact responses for QBPZTR: (a) $\Re_{xx}$, (b) deformed shape of QBPZTR at the corresponding mode.

conducted to build a simple impact model, based on the two key assumptions established by experimental observation described above in this section.

Assumption 1. The coefficient of restitution at the contact point is constant over time, for given foot and terrain materials. This implies a conventional CoR relationship at the impact point,

$$\dot{x}^+ = -\alpha \dot{x}^- \qquad (10)$$

where α is a constant representing a coefficient of restitution.

Assumption 2. Structural motion right after the impact is determined by the dominant mode shape associated with the location and direction of the impact.

Assumption 2, in particular, is a simplification of more ideal approaches for modeling impact as a delta function influencing all modes. However, as was observed experimentally in the previous section, the majority of robot behavior is observed to be associated with a single mode. Attempting to identify the influence on other, comparatively difficult to observe modes, and then implement that behavior in simulation is prone to numerical error, while isolating dominant mode behavior is found to produce more consistent predictions of robot behavior.

With these empirically motivated assumptions, we derive the CoR matrix defining impact motion. Let $\mathbf{J_I}$ be an impact impulse over contact duration t^- to t^+, or

$$\mathbf{J_I} = \int_{t^-}^{t^+} \mathbf{F_I} \, \mathrm{d}t. \qquad (11)$$

Using $\mathbf{\Phi}$, the modal transformation matrix, the impact impulse in modal coordinates can be obtained as

$$\mathbf{j_I} = \mathbf{\Phi}^{-1} \mathbf{J_I} = \int_{t^-}^{t^+} \mathbf{\Phi}^{-1} \mathbf{F_I} \, \mathrm{d}t = \int_{t^-}^{t^+} \mathbf{f_I} \, \mathrm{d}t. \qquad (12)$$

For a model consisting of m modes, the impact impulse in modal coordinates can be expressed as individual elements,

$$\mathbf{j_I} = [j_{I,1} \; j_{I,2} \; \cdots \; j_{I,m}]^{\mathrm{T}}. \qquad (13)$$

Let the inertial contribution to motion by each mode be represented by a set of parameters, $\eta_1, \eta_2, \ldots, \eta_i, \ldots, \eta_m$, with units of $1/\text{mass}$; then the modal momentum change during impact can be related to the modal coordinates as follows,

$$\dot{\mathbf{q}}^+ - \dot{\mathbf{q}}^- = [\eta_1 j_{I,1} \; \eta_2 j_{I,2} \; \cdots \; \eta_m j_{I,m}]^{\mathrm{T}}. \qquad (14)$$

Based on Assumption 2, let the kth mode be dominant and govern structural motion right after the impact, then

$$\begin{aligned} \dot{\mathbf{q}}^+ - \dot{\mathbf{q}}^- &= [0 \, 0 \, \cdots \, 0 \; \dot{q}_k^+ - \dot{q}_k^- \; 0 \, \cdots \, 0]^{\mathrm{T}} \\ &= [0 \, 0 \, \cdots \, 0 \; \eta_k j_{I,k} \; 0 \, \cdots \, 0]^{\mathrm{T}}. \end{aligned} \qquad (15)$$

This can be transformed back to the physical coordinates,

$$\begin{aligned} \dot{\mathbf{x}}^+ - \dot{\mathbf{x}}^- &= \mathbf{\Phi}(\dot{\mathbf{q}}^+ - \dot{\mathbf{q}}^-) \\ &= \mathbf{\Phi}[0 \, 0 \, \cdots \, 0 \; \dot{q}_k^+ - \dot{q}_k^- \; 0 \, \cdots \, 0]^{\mathrm{T}} \\ &= \phi_k \eta_k j_{I,k} \end{aligned} \qquad (16)$$

where ϕ_i is the ith column vector in the transformation matrix,

$$\mathbf{\Phi} = [\phi_1 \; \phi_2 \; \cdots \; \phi_i \; \cdots \; \phi_m]. \qquad (17)$$

Equation (16) can be expressed as follows,

$$\dot{\mathbf{x}}^+ - \dot{\mathbf{x}}^- = \phi_k \eta_k j_{I,k} = \frac{\phi_k}{\phi_{k,c}} \phi_{k,c} \eta_k j_{I,k} \qquad (18)$$

where c indicates the index of the contact foot and $\phi_{k,c}$ is the cth element of the column vector ϕ_k. By Assumption 1, the CoR at the contact foot is consistent,

$$\frac{\dot{x}_c^+}{\dot{x}_c^-} = \alpha. \qquad (19)$$

Here, α represents the CoR at the contact foot. The above can also be written as follows,

$$\dot{x}_c^+ - \dot{x}_c^- = (\alpha - 1)\dot{x}_c^- \qquad (20)$$

in the row in (16) corresponding to x_c, inserting (19) gives,

$$\phi_{k,c} \eta_k j_{I,k} = (\alpha - 1)\dot{x}_c^-. \qquad (21)$$

If (21) is substituted into (18), the following can be obtained,

$$\dot{\mathbf{x}}^+ - \dot{\mathbf{x}}^- = \frac{\phi_k}{\phi_{k,c}}(\alpha - 1)\dot{x}_c^-. \qquad (22)$$

Let

$$\beta_c = \frac{\phi_k}{\phi_{k,c}}(\alpha - 1). \qquad (23)$$
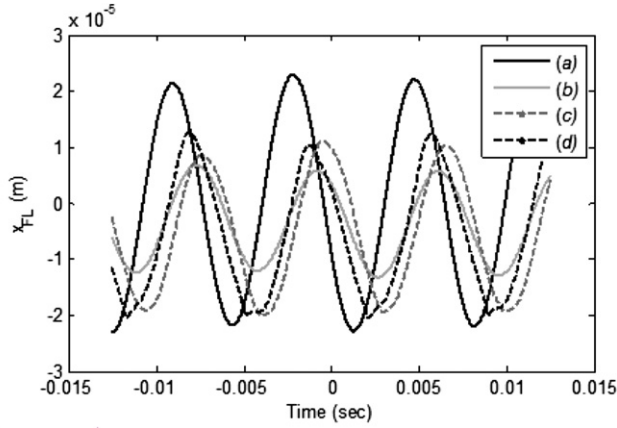
Figure 14. Experimental data for the vertical foot velocity with the silicon ground pad, varying the gap from the ground pad, d, and the voltage input, V_{in}. (a) $d > 3$ cm, $V_{in} = 10$ V; (b) $d = 25$ μm, $V_{in} = 3$ V; (c) $d = 25$ μm, $V_{in} = 6$ V; (d) $d = 25$ μm, $V_{in} = 10$ V.

Then, substituting equation (21) into equation (2), the change in physical coordinate velocity after impact can be written as a function of the contact point velocity at impact,

$$\dot{\mathbf{x}}^+ - \dot{\mathbf{x}}^- = \beta_c \dot{x}_c^- . \tag{24}$$

Alternatively to the above form, a matrix form of the CoR can be obtained which is easier to incorporate into numerical simulation models. From (24),

$$\dot{\mathbf{x}}^+ - \dot{\mathbf{x}}^- = \frac{\phi_k}{\phi_{k,c}}(\alpha - 1)\dot{x}_c^-$$

$$= \begin{bmatrix} \dfrac{\phi_{k,1}}{\phi_{k,c}} & \dfrac{\phi_{k,2}}{\phi_{k,c}} & \cdots & \dfrac{\phi_{k,c}}{\phi_{k,c}} & \cdots & \dfrac{\phi_{k,m}}{\phi_{k,c}} \end{bmatrix}^{\mathrm{T}}$$

$$\times (\alpha - 1)\dot{x}_c^- . \tag{25}$$

Let $c = 1$, then

$$\dot{\mathbf{x}}^+ = \begin{bmatrix} \alpha & 0 \\ \dfrac{(\alpha - 1)}{\phi_{k,1}} \begin{bmatrix} \phi_{k,2} & \phi_{k,3} & \cdots & \phi_{k,m} \end{bmatrix}^{\mathrm{T}} & \mathbf{I}_{5 \times 5} \end{bmatrix} \dot{\mathbf{x}}^- . \tag{26}$$

Let

$$\beta_{c'} = \frac{(\alpha - 1)}{\phi_{k,1}} \begin{bmatrix} \phi_{k,2} & \phi_{k,3} & \cdots & \phi_{k,m} \end{bmatrix}^{\mathrm{T}} . \tag{27}$$

Then, from (25),

$$\dot{\mathbf{x}}^+ = \begin{bmatrix} \alpha & 0 \\ \beta_{c'} & \mathbf{I}_{(m-1) \times (m-1)} \end{bmatrix} \dot{\mathbf{x}}^- = \mathbf{R}_{\mathrm{CoR}} \dot{\mathbf{x}}^- \tag{28}$$

where $\mathbf{R}_{\mathrm{CoR}}$ represents the CoR matrix and this is applied to the dynamic model for adjusting the instant velocities of the system to approximate the impact behavior.

3.5. Small-scale force identification

A final factor in modeling micro-robotic foot–ground interactions is the existence and magnitude of small-scale forces. For the HBPZTR, the smaller of the two robots, small-scale forces are quantified and included in the simulation model. In
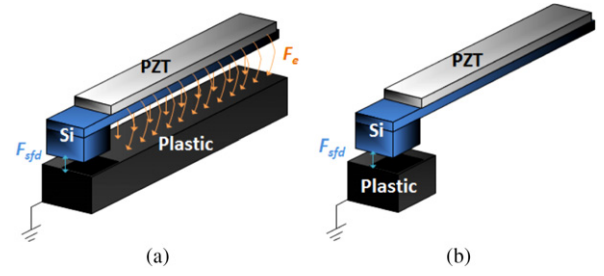
Figure 15. Tested ground pads for HBPZTR: (a) long pad and (b) short pad.
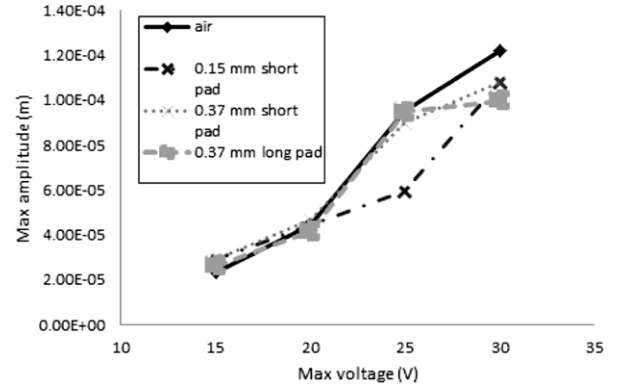
Figure 16. Existence of small-scale forces implied from experimental analysis on different gaps and pads.

contrast, small-scale forces were not observed to be significant in the much more massive QBPZTR. Intermediate distances of about 20–40 μm between a foot surface and the ground can be obtained by adjusting the height of the robots using the vertical micro-positioner shown in figure 3. At this particular range of the gap, a foot does not successfully make contact with the ground, but small-scale forces affect the system dynamics in a measurable way. Figure 14 shows a comparison of experimental data sets for the HBPZTR over various voltage inputs and two inter-surface gaps: 3 cm and 25 μm. It can be seen that the magnitude of the foot motion decreases when the distance between the foot and the ground is small, when comparing cases with the same voltage.

Testing with various ground pads, shown in figure 15, implied that at least two small forces significantly affect the foot motion. Observed effects are consistent with those forces being a squeeze-film damping force and an electrostatic force, arising as shown in figure 15(a). Squeeze-film damping is assumed to be localized at the robot foot and electrostatic effects distributed over the leg as associated with the input voltage.

To test this assumption, a second ground configuration with a short ground pad, shown in figure 15(b), was inserted and trends in motion amplitude measured experimentally, as shown in figure 16, in an attempt to isolate the various effects. Cases shown include motion without a ground pad, motion over a short pad with a smaller and larger initial gap, and for a long ground pad at the larger initial gap. The voltage is gradually increased, though without reaching the point of contact during leg motion.
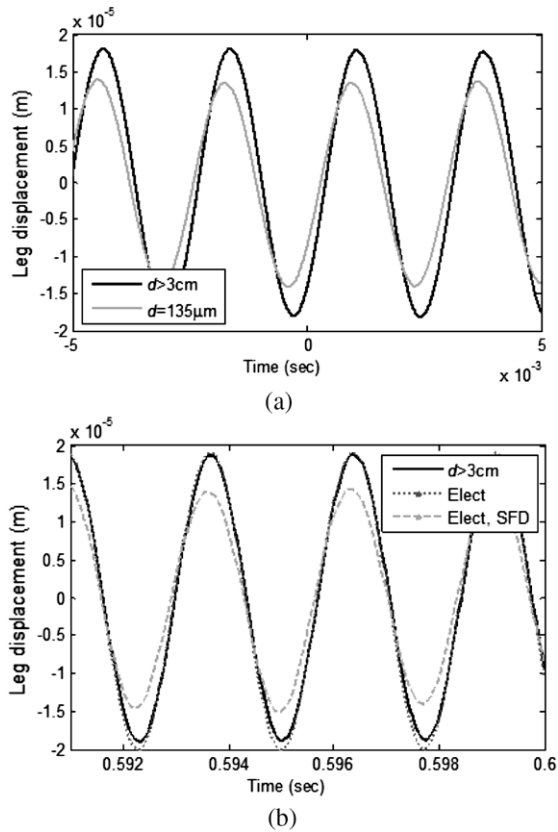
Figure 17. Validation of small-scale forces between the foot and the ground using a 10 V voltage input: (a) experimental data and (b) simulation results.

As figure 16 shows, in all cases as the voltage increases there is a smaller increase in amplitude when the leg is in close proximity to the ground pad compared to its free motion in air. This is attributed to the fact that as the maximum voltage input (MVI) increases, the resulting smaller minimum gap between the foot and the ground pad induces a greater influence of small-scale forces, predominantly squeeze-film damping. This partially offsets the increased amplitude due to increasing MVI. Comparing the two cases using the same short ground pad but different initial gaps, there is a large difference at 25 V MVI, which indicates that squeeze-film damping has begun to significantly act in the case of the 0.15 mm initial gap. By 30 V MVI, the difference between the two cases is smaller, as squeeze-film damping acts significantly in both cases. Comparing two cases using the same initial gap but different length pads, the case using a long pad shows a slightly larger amplitude at 25 V MVI, attributed to additional electrostatic forcing. This then returns to a comparable amplitude at 30 V MVI, which is believed to be a result of squeeze-film damping again becoming the dominant nonlinear effect when the gap becomes very small between the leg and the ground.

Additional comparisons between experimental and simulation results in time-domain responses are shown in figure 17. Simulation studies implied that the reduction in magnitude is due to squeeze-film damping and slight shifting of the sinusoidal output is mostly due to electrostatics, as shown in the figure. Using an experimental comparison with the

simulation results, each small-scale force has been quantified and added to the model using functional forms previously developed by Yeh *et al* [19] and used by the authors in cantilever impact experiments [18]. However, it is worth noting that, at the current robot scale, electrostatic effects are much smaller than either squeeze-film damping or piezoelectric forcing, and primarily of interest for robots with smaller dimensions.

4. Results and model validation

The dynamic models with the proposed impact model for both test robots were validated using further experimental comparisons. Simulation responses were generated using the modal vibration model from (3), impact behavior from (28), and small-scale models from [18] optionally inserted for $\sum \mathbf{F_{SS}}$ in (4). Initial conditions were set to zero, though simulated behavior in this section is compared to experiments only after initial transient effects have died out, at least after a simulation time of 0.15 s. The implied boundary conditions for the modal model were zero displacement and velocity at the base of the wire tethers to the robots, though in the real setup there is some possibility of deformation of the wires at the fixtures. All structural parameters were obtained from system identification of robot vibration in the air and impact parameters and small-scale force parameters obtained by the identification methods described in section 3.

Figure 18 shows the sample simulated to experimental comparisons for the QBPZTR, which is the response of five different points for the same excitation. Figure 19 shows a comparison for the HBPZTR at a single point (the actuated leg) for three different inputs. Validation is focused on the comparison of time-series responses. However, it is not easy to directly compare the simulation result and the experimental data despite using periodic voltage inputs, since the resulting impact response does not repeat over a single period, but rather over several successive periods, and there is significant random variation. Nonetheless, it can be seen for both robots that the overarching periods and amplitudes of the simulation and experimental responses are consistent and similar to each other. Hence, using the feature of periodic voltage inputs, the time-series responses have been mapped into circular coordinates, as shown in figures 18 and 19. One circular rotation indicates one periodic cycle of the input and the distance from the origin indicates physical height from the ground. This plot provides a better understanding in the comparison of trends and behaviors of system responses over various disturbances, including impact with the ground. For the QBPZTR, as shown in figure 18, the response amplitudes of the bouncing foot and most other feet are in good agreement, with the exception being the fore-right foot. The impact behavior at the bouncing foot is captured especially well (figure 18(a)), showing a very similar repetitive trend in magnitude and oscillation in air after break-off in simulation as in experimental testing. Errors in amplitude at the other feet and the body can also be seen to be within the standard deviation between individual robot experiments, as shown in the insets of the respective plots in figure 18.
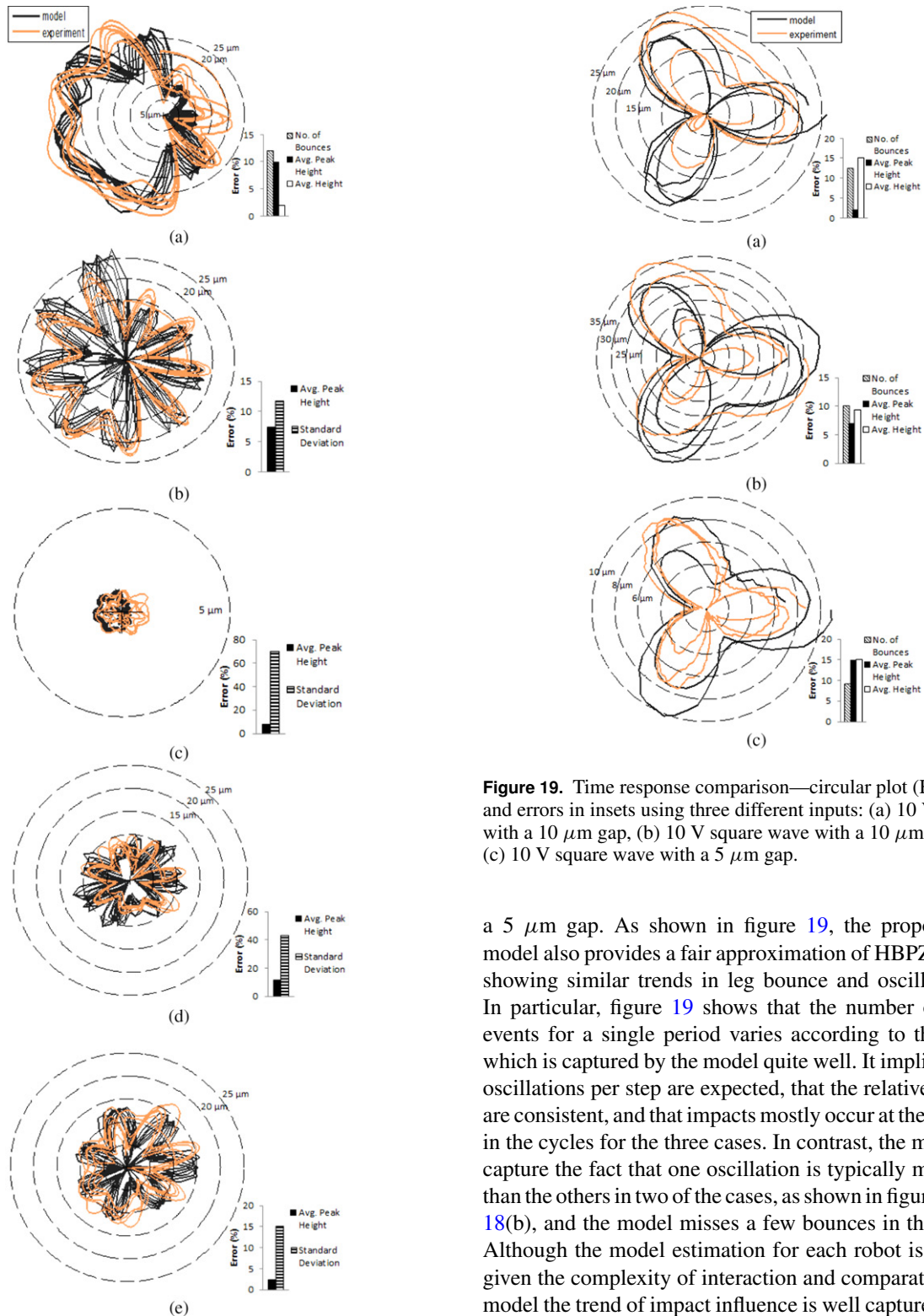
Figure 18. Time response comparison—circular plot (QBPZTR) and errors in insets: (a) fore-left leg (bouncing leg), (b) fore-right leg, (c) center of body, (d) hind-left leg and (e) hind-right leg.

For the HBPZTR, experimental validation was conducted by comparing responses at the bouncing foot using three different test cases: 10 V sine input with a 10 μm gap, 10 V square input with a 10 μm gap, and 10 V square input with

Figure 19. Time response comparison—circular plot (HBPZTR) and errors in insets using three different inputs: (a) 10 V sine wave with a 10 μm gap, (b) 10 V square wave with a 10 μm gap and (c) 10 V square wave with a 5 μm gap.

a 5 μm gap. As shown in figure 19, the proposed impact model also provides a fair approximation of HBPZTR motion, showing similar trends in leg bounce and oscillation in air. In particular, figure 19 shows that the number of bouncing events for a single period varies according to the test case, which is captured by the model quite well. It implies that three oscillations per step are expected, that the relative amplitudes are consistent, and that impacts mostly occur at the same points in the cycles for the three cases. In contrast, the model fails to capture the fact that one oscillation is typically much smaller than the others in two of the cases, as shown in figures 19(a) and 18(b), and the model misses a few bounces in the third case. Although the model estimation for each robot is not perfect, given the complexity of interaction and comparatively simple model the trend of impact influence is well captured, as shown in these figures.

For the HBPZTR, the existence of small-scale forces and their influence on motion was validated by comparing simulation results with and without such forces and the experimental data, as shown in figure 20. The diagrams show the relative levels of three quantified descriptions of vertical motion: average leg height, number of bounces over a fixed time period, and peak leg height. In each of the three scenarios discussed above, and by each of the three criteria, simulations
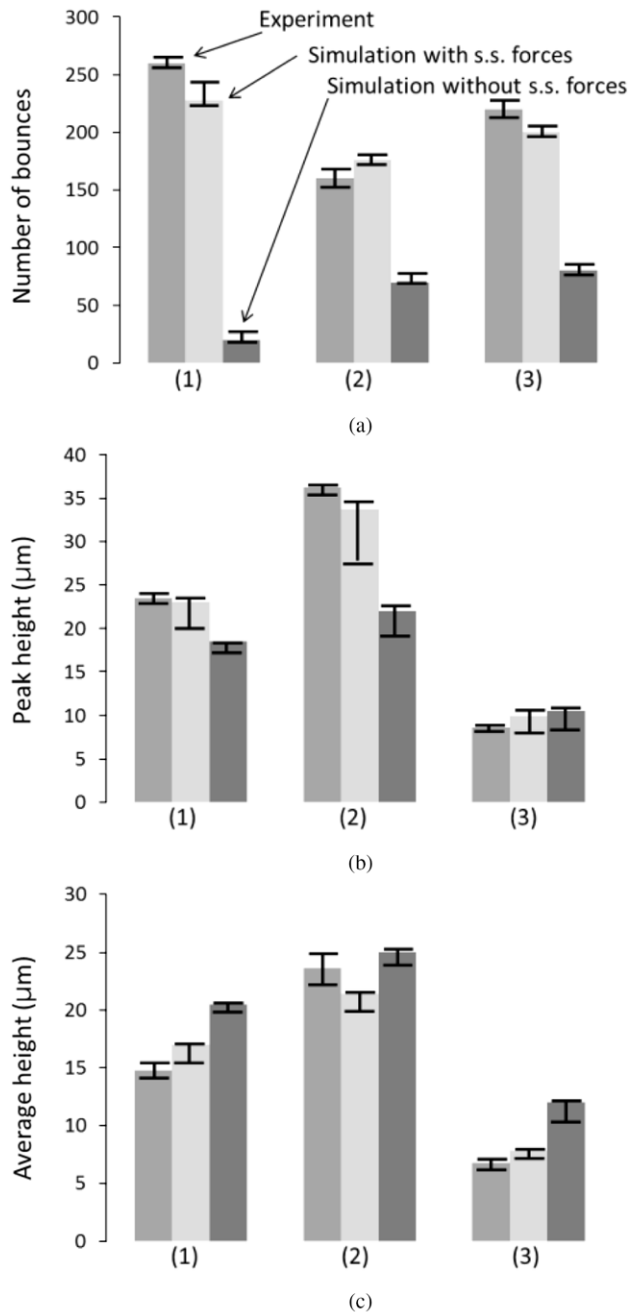
Figure 20. Comparison of experimental impact behaviors over 1 s to simulated behavior with and without small-scale forces: (1) 10 V sine wave with a 10 μm gap, (2) 10 V square wave with a 10 μm gap, (3) 10 V square wave with a 5 μm gap. (a) Number of bounces, (b) maximum peak heights, (c) average heights.

with small-scale forces included came much closer to matching experimental data than simulations without. This is crucial for modeling full gait motion of walking robots, since lateral leg actuation contributions to locomotion of robots are made mostly when there is contact between the leg and the ground. Full gait simulation, though, is beyond the scope of this paper and is future work.

While average results for experimental and simulated foot response are not in complete agreement, they generally agree to within combined uncertainties in the results.

Moreover, for the smaller HBPZTR, results agree only when including small-scale forces. As shown in figure 20 and table 3, there is significant variation from case to case, but across various test scenarios trends in bounce frequency, peak leg height and average leg height are generally very well captured, with average errors near 10%. This discrepancy can be compared visually in figure 20 to uncertainty in the experimental and simulation results, shown by error bars. Uncertainty in the simulation results was obtained by using the maximum and minimum values of the CoR's parameter determined during the system identification process, with respect to which the simulation was found to have the highest sensitivity among identified parameters. In almost all scenarios, simulations that include small-scale forces fall within combined uncertainty for the system, while simulations that do not contain small-scale forces have much greater differences. This is especially true for predictions of bouncing, where neglecting small-scale effects causes bouncing to be consistently under-predicted. There are a few situations that fall out of agreement even with small-scale forces, namely bouncing frequency with a sine input and average leg height with a square input and larger 10 μm gap. These could be cases where the matrix model for CoR behavior is too much of an oversimplification, or there could be impact phenomena that remain to be incorporated. However, relative to previous works on micro-scale impact, the model for impact is effective in quantifying an unusually large number of factors.

5. Conclusions and future work

Using two different prototype micro-robots operated with bulk PZT ceramics, this paper proposes a modeling procedure for the robot foot–terrain interactions. Structural dynamics were modeled by conventional modal analysis and small-scale forces in a lumped-parameter fashion. This simplifies system identification to a limited number of parameters, while providing fairly good reproduction of motion considering the variety of unknown factors that might significantly affect the system dynamics, such as exact geometries or material properties of the contact surfaces.

Impact behavior was analyzed using relatively simple processing of experimental data and certain consistent trends were observed. They indicate that impact behavior is related closely to the modal characteristics of the mechanical structure, as would be expected, but also showed a close match with one major mode shape in each robot. In order to describe this theoretically, an impact model is established with a CoR matrix that is based on the two fundamental assumptions: first, that a single CoR at the contact foot is constant over various voltage input signals for a specific ground surface and, second, that instant motion of a continuous structure at the moment of impact is governed by a dominant mode shape that is determined by the location of the impact. Through comparison to experimental results, it was shown that a single mode shape was adequate to approximate the system responses to instantaneous impact disturbance. For the HBPZTR, experimental observation also revealed a few small-scale contact forces having a significant influence on dynamic

Table 3. Numerical comparisons between model and measured data.

| | 10 V sine wave input/10 μm gap | | 10 V square input/10 μm gap | | 10 V square input/5 μm gap | | |
	Exp.	Model	Exp.	Model	Exp.	Model	Avg. error (%)
$\dot{N}_B$ [a]	260	228	160	176	220	200	−6
A_{max} [b]	23.5	23.0	36.2	33.7	8.6	9.9	−3
A_{avg} [c]	14.8	17.0	23.6	21.4	6.8	7.8	2

[a] Number of bounces per second. [b] Peak height (μm). [c] Average height (μm).

response. This occurred within an approximately 30 μm gap between the foot and the ground for a robot less than 0.2 g in mass. Observing system responses over various gaps between surfaces, ground pads with different lengths to isolate each short-range force, and varying static voltages applied to them, such forces were quantified and incorporated into the model. Further experimental validation shows that the proposed model for each prototype micro-robot provides relatively good approximations to a variety of test environments with different voltage inputs and gaps between surfaces.

As a critical limitation of the work in this paper, it should be noted that this impact model might not be directly applicable to different cases, such as multi-point contact interactions or other mechanical devices. For such cases, impact behavior would be probably much more complicated and it might be represented by more than two mode shapes due to multiple points of impact disturbance. However, it is also possible that some combinations of the locations of impact disturbance may significantly induce a single mode shape at the instant of impact events. Thus, analysis on both major mode shapes and experimental investigation should be conducted to determine how many CoR matrices are needed for all combinations of locations of impact disturbances according to the number of legs and gait sequences, and which mode shapes should be chosen for each combination to construct a CoR matrix for it. Unfortunately, it is hardly possible to test multiple contact point interactions with the current test setups. This is because it is extremely hard to achieve the same distance between all feet and the ground since both devices are suspended with elastic copper wires and it cannot be guaranteed that the devices are perfectly horizontal over the ground. Another significant limitation in this paper is that the influence of the copper wires on impact responses is relatively large despite their thinness, due to the small mass of the test devices. Thus, we had to filter out a very low resonance mode, which is supposed to be related to the wires. This might result in loss of information on impact behavior.

In the future, it is hoped that an understanding of impact behavior of small walking robots will aid in the design of energy efficient walking or running gaits. The most significant obstacles to practical application of terrestrial micro-robots in complex environments are arguably ensuring system reliability and operating under very strict power budgets. While impact modeling may help reduce stresses on micro-robots, the primary path to improving robot structural robustness is likely through new micro-fabrication materials and processing. Energy consumption, on the other hand, can potentially be reduced dramatically if energy can be conserved from step to step in dynamic walking gaits, as proposed for a variety of macro-robotic systems. The model for foot impact developed in this paper should aid in the development of leg input sequences and gait designs that sustain desirable motion over many steps, and with minimal input energy, if the model can be extended to multiple foot impacts.

Hence, for future work, new test setups are being designed for multi-point contact interaction tests and elimination of the influence of wire bonding to allow fully fledged dynamic walking tests. As an idea, conductive ground pads or electric fields can be used as an alternative power supply instead of direct connection with wires. Another idea is the application of a micro-force sensor attached to each foot, sensing the relative change in response to estimate the force transmitted from each leg to the ground while various gait sequences are designed and tried. These may be conducted in future works to expand the impact model proposed in this paper to more generic cases in other micro-robotic structures.

Acknowledgments

References

[1] Hollar S, Flynn A, Bellew C and Pister K S J 2003 Solar powered 10 mg silicon robot *Proc. IEEE Int. Conf. MEMS* pp 706–11

[2] Ebefors T, Mattsson J U, Kälvesten E and Stemme G 1999 A walking silicon micro-robot *Proc. Transducers '99* pp 1202–5

[3] Mohebbi M H, Terry M L, Böhringer K F, Kovacs G T A and Suh J W 2001 Omnidirectional walking microrobot realized by thermal microactuator arrays *Proc. ASME Int. Mechanical Engineering Congress and Exposition* pp 167–73

[4] Murthy R, Das A and Popa D O 2008 ARRIpede: an assembled micro crawler *Proc. 8th IEEE Conf. Nanotechnology* pp 833–6

[5] Donald B R, Levey C G and Paprotny I 2008 Planar microassembly by parallel actuation of MEMS microrobots *J. Microelectromech. Syst.* **17** 789–808

[6] Fukuda T, Kawamoto A, Arai F and Matsuura M 1994 Mechanism and swimming experiment of micro mobile robot in water *ICRA'94* vol 1, pp 814–9

[7] Kosa G, Shoham M and Zamoor M 2007 Propulsion method for swimming microrobots *IEEE Trans. Robot.* **23** 137–50

[8] Watson B, Friend J, Yeo L and Sitti M 2009 Piezoelectric ultrasonic resonant micromotor with a volume of less than 1 mm^3 for use in medical microrobots *ICRA'09* pp 2225–30

[9] Wood R J, Finio B, Karpelson M, Perez-Arancibia N O, Sreetharan P and Whitney J P 2011 Challenges for micro-scale flapping wing micro-air vehicles *Proc. SPIE* **8373** 83731J

[10] Pulskamp J S, Polcawich R G, Rudy R Q, Bedair S S, Proie R M, Ivanov T and Smith G L 2012 Piezoelectric PZT MEMS technologies for small-scale robotics and RF applications *MRS Bull.* **37** 1062–70

[11] Baisch A T, Sreetharan P S and Wood R J 2010 Biologically-inspired locomotion of a 2 g hexapod *IROS'10 (Taipei, Taiwan)* pp 5360–5

[12] Adams G G 1997 Imperfectly constrained planar impacts—a coefficient-of-restitution model *Int. J. Impact Eng.* **19** 693–701

[13] Lankarani H M and Nikravesh P E 1994 Continuous contact force models for impact analysis in multibody systems *Nonlinear Dyn.* **5** 193–207

[14] Hurmuzlu Y and Marghitu D B 1999 Rigid body collisions of planar kinematic chain with multiple contact points *Int. J. Robot. Res.* **13** 82–92

[15] Lee S I, Howell S W, Raman A and Reifenberger R 2002 Nonlinear dynamics of microcantilevers in tapping mode atomic force microscopy: a comparison between theory and experiment *Phys. Rev.* B **66** 115409

[16] Krylov S and Barnea D I 2005 Bouncing mode electrostatically actuated scanning micromirror for video applications *Smart Mater. Struct.* **14** 1281–96

[17] LaRose R P and Murphy K D 2009 Impact dynamics of MEMS switches *Nonlinear Dyn.* **60** 327–39

[18] Ryou J H and Oldham K R 2012 Model identification for impact dynamics of a piezoelectric microactuator *J. Micromech. Microeng.* **22** 115002

[19] Yeh R, Hollar S and Pister K S J 2002 Design of low-power silicon articulated microrobots *J. Micromechatronics* **1** 191–203

[20] Inman D J 2000 *Engineering Vibration* 2nd edn (Englewood Cliffs, NJ: Prentice-Hall) p 495

[21] Wagg D J 2006 A note on coefficient of restitution models including the effects of impact induced vibration *J. Sound Vib.* **300** 1071–8